

Performance of the ATLAS Hadronic Endcap Calorimeter in Particle Beams

Candidacy Paper

Matt Dobbs¹

*University of Victoria,
Victoria, Canada.*

April 28, 1999

Abstract

ATLAS is one of two general purpose detectors designed to exploit the physics potential of the Large Hadron Collider (LHC) at CERN. The ATLAS calorimetry system includes the Hadronic Endcap, which is a liquid argon sampling calorimeter that will provide coverage for hadronic showers in the forward region of the ATLAS detector. The first Hadronic Endcap modules built to the final ATLAS specifications were tested in particle beams at CERN in April 1998. A brief introduction to hadronic calorimetry is presented followed by an analysis of the calorimeter's response and resolution to particle beams over an energy range of 20 to 180 GeV. The electron energy resolution is parameterized as $\frac{\sigma}{E} = \frac{22.0 \pm 0.01\%}{\sqrt{E_0}} \oplus 0.0 \pm 0.2\% \oplus \frac{0.54 \pm 0.02}{E}$ where E_0 is expressed in GeV. The pion energy resolution (with pre-subtracted noise) is parameterized as $\frac{\sigma}{E} = \frac{78 \pm 2\%}{\sqrt{E_0}} \oplus 5.0 \pm 0.3\%$.

¹Matthew.Adam.Dobbs@Cern.CH

1 Introduction

High energy particle physics is the study of the fundamental forces of nature which govern the interactions between radiation and the ultimate constituents of matter. The distance scale at which an experiment is able to probe is related to particle momentum p by the de Broglie wavelength $\lambda = h/p$ where h is the Planck constant 6.63×10^{-34} J s. Experiments of higher energy are necessary to probe smaller scales of matter. The Large Hadron Collider (LHC) currently under construction at the European Laboratory for Particle Physics (CERN) in Geneva, Switzerland is the next generation of high energy collider. It will access energy regimes (and therefore distance scales) never before realized in terrestrial experiments.

At colliders such as the LHC, detectors attempt to the products of particle collisions. The energy of particles produced in these collisions is an important quantity to measure. At the LHC, the energy of most particles will be measured using calorimetry systems.

ATLAS is one of two general purpose detectors being constructed to operate at the LHC. The Hadronic Endcap Calorimeter (HEC) will operate as part of the calorimetry system of the ATLAS detector. An understanding of the performance characteristics of the calorimeter is necessary to assess its contributions to the ATLAS detector capabilities and to ensure the HEC performs as expected from its design. In this paper the performance of the HEC in particle beam tests is presented.

Sections 2 & 3 present the LHC collider and ATLAS detector. A brief review of particle interactions, cascades, and general calorimetry follows. The HEC calorimeter and beam test experimental setup are described in sections 6 & 7. The evaluation of the calorimeter's response to electrons, muons and hadrons, and resolution to electrons and hadrons are treated in Sections 8 to 10. Considerations for the reconstruction of hadronic showers with the HEC in the ATLAS environment are briefly presented in Section 11.

Sections 8 & 10 (except 10.4.1) of the analysis described in this candidacy are published as an ATLAS Internal Note and Hadron Endcap Internal Note written by M. Dobbs, D. O'Neil and M. Lefebvre, see [1].

2 The Large Hadron Collider

The Large Hadron Collider (LHC) will achieve proton-proton collisions at a center of mass energy of 14 TeV with beam crossing points of unsurpassed brightness (luminosity). This will allow the LHC to probe the energy scales at which electroweak symmetry breaking scenarios (which may include the as yet unobserved Higgs boson particle) ² are expected to manifest themselves.

²Gauge boson (spin 1 particles, i.e. W^\pm , Z^0 and the photon) masses violate gauge invariance and thus are not allowed in a gauge invariant theory. The W^\pm & Z^0 masses are believed to arise from spontaneous symmetry breaking via the Higgs mechanism wherein the symmetry is present in the underlying theory, but hidden. Nevertheless, the Higgs mechanism doesn't fully solve the problem, since it postpones it to a higher energy scale. Theoretical considerations dictate the underlying physics of the electroweak symmetry breaking should reveal itself at the multi-TeV scale. For more information on electroweak symmetry breaking and the Higgs mechanism, see [2].

The Large Hadron Collider (LHC) will supersede the Large Electron Positron (LEP) collider currently running at CERN. The 27 km LEP tunnel will house the LHC's two superconducting magnetic channels which accelerate the protons. The LHC magnet coils are made of copper-clad niobium-titanium cables which produce a magnetic field of 8.36 T and operate at 1.9 K. They represent the forefront of superconducting magnet technology.

The *luminosity* of a collider is proportional to the number of collisions realized per second. When multiplied by the cross section of a physics process (expressed as an area), the luminosity gives the event rate. Rare processes require high luminosities to be measurable. Because the de Broglie wavelength decreases like $1/E$, the cross section of processes of interest decrease like $1/E^2$. Thus at higher energy, generally speaking, the luminosity of a collider should increase in proportion to E^2 in order to maintain a similar rate for rare events. The LHC energy is about a factor 10 times that of LEP which has a luminosity of $\sim 10^{32} \text{ cm}^{-2}\text{s}^{-1}$, hence a factor of about 100 is required in luminosity. At the LHC the two superconducting channels will be filled with 2835 bunches of 10^{11} particles each, achieving the design luminosity of $10^{34} \text{ cm}^{-2}\text{s}^{-1}$. Bunch crossings will occur every 25 ns. This crossing rate represents a tradeoff between event multiplicity (number of simultaneous events in a single bunch crossing, referred to as *pileup*) which grows and electronic noise which decreases with the bunch crossing rate.

3 Overview of the ATLAS Detector

The Canadian particle physics community is heavily involved in the ATLAS experiment,³ one of two general purpose detectors which will exploit the physics potential of the LHC. The ATLAS detector, like the LHC, is entering its construction phase.

Proton-proton collisions produced by the LHC will be reconstructed in the ATLAS detector. An ideal detector would reconstruct the 4 momentum (E, \vec{p}) of all particles produced in these multi-particle events. The design of the ATLAS detector is subject to many constraints. Among them, the LHC's 25 ns bunch crossing rate necessitates fast signal readout, the dimensions of the detector must be large to perform measurements on high energy particles, and the high particle multiplicity requires a highly granular detector. Furthermore, the ATLAS detector must operate in a high radiation environment, especially in the forward regions.

The ATLAS detector is composed of many subdetectors, each optimized to detect some aspect of a collision event. The overall structure consists of subdetectors for tracking and particle identification located closest to the interaction point followed by the calorimetry system and then by muon detectors.

The layout of the ATLAS detector is shown in Figure 1. The exterior dimensions of the ATLAS detector are defined by the muon spectrometer. The outer chambers of the barrel extend to a radius of 11 m (making ATLAS about 8 stories high). The barrel toroid

³Canadian institutions involved in the ATLAS collaboration include: the University of Alberta, University of Carleton/C.R.P.P., Université de Montréal, University of Toronto, TRIUMF, University of British Columbia, University of Victoria, and York University.

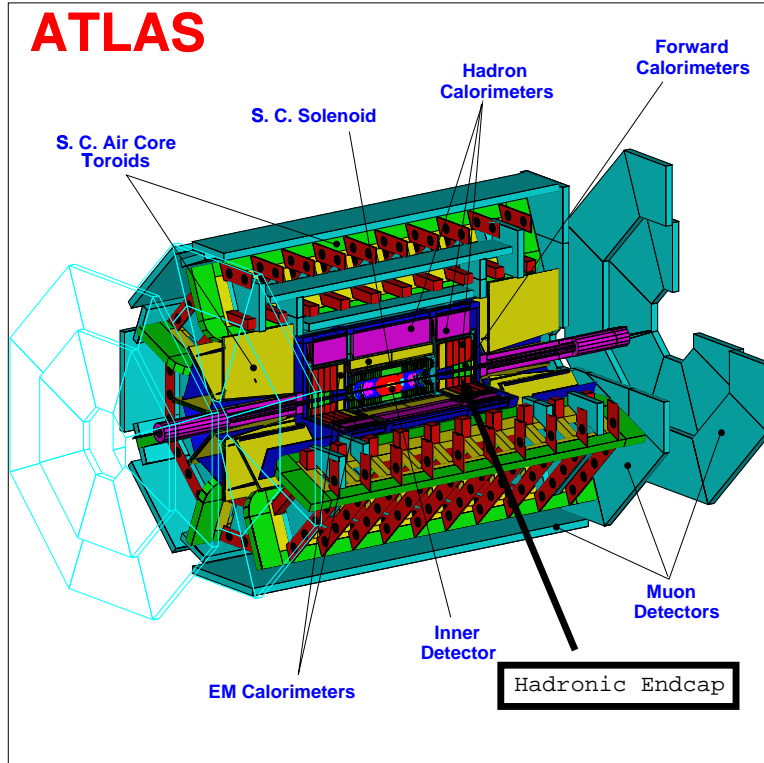


Figure 1: The overall layout of the ATLAS detector. The total height (diameter) is about 22 m. The Hadronic Endcap Calorimeter is indicated.

coils extend longitudinally 13 m from the interaction point on either side and the outermost forward muon chambers are mounted on the cavern wall 21 m longitudinally from the interaction point. The total weight of the ATLAS detector is about 7000 tons.

The magnetic fields in the detector⁴ are produced by a 2 T inner superconducting solenoid around the inner detector cavity and eight large independent superconducting air-core toroids (4.2 T peak field) arranged outside the calorimetry.

The inner detector, located closest to the interaction point in a cylinder of radius 1.15 m and length 6.8 m, employs a combination of discrete high-resolution pixel and strip detectors in the inner part of the tracking volume and continuous straw-tube tracking detectors with transition radiation capability in the outer part. The sub-detector performs pattern recognition, momentum and vertex measurements, and enhanced electron identification.

The calorimetry system, shown in Figure 2, surrounds the inner detector and plays a central role in ATLAS. It is designed to trigger on and provide energy and directional mea-

⁴Magnetic fields in particle detectors serve to curve the particle's path by an amount inversely proportional to the particle's momentum. By measuring a particle's curvature (with wire chambers for example) its momentum can be inferred.

ATLAS Calorimetry (Geant)

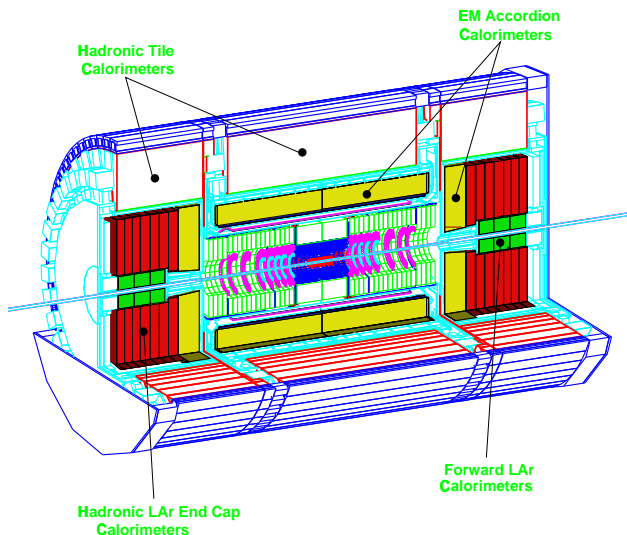


Figure 2: A three dimensional view of the ATLAS calorimeter system [3]. The total length of the system shown is about 13 m.

measurements of electrons, photons, jets⁵ and missing transverse energy⁶.

Liquid argon (LAr) technology is chosen for the regions of the calorimetry system closest to the beam, mainly due to its fast signal readout capabilities, radiation hardness, and ease of calibration. The LAr calorimetry is contained in a cylinder with outer radius 2.25 m and longitudinal length ± 6.65 m.

Highly granular lead/LAr electromagnetic sampling calorimeters with “accordion-shaped” electrodes are used in the pseudorapidity interval⁷ $|\eta| < 3.2$ (about 4.7° from the beam-line). A central cryostat houses the barrel electromagnetic calorimeter and the inner superconducting solenoid. LAr technology is also used for the Hadronic Endcap calorimeter (the focus of this paper), which shares a cryostat with the electromagnetic endcaps and the special copper/tungsten/LAr forward calorimeters which extend the η coverage down to ± 4.9 .

⁵Jets are initiated by quarks attempting to leave the interior of a hadron, causing quark-antiquark pairs to be created. New hadrons are formed by the recombination of the quarks and antiquarks. A narrow spray of hadrons known as a *jet* are formed in this way by very energetic quarks.

⁶Neutrinos (which undergo only the weak force) are essentially undetectable on an event by event basis in high energy collider detectors. The momentum of all other particles in an event are measured and conservation of momentum of the whole event is employed to infer the “missing momentum” which is associated primarily with neutrinos. For the case of hadron colliders, the subprocess is boosted longitudinally with respect to the lab frame. This boost cannot be directly measured since many particles escape down the beam-pipe carrying longitudinal momentum, hence conservation is applied to the transverse momentum only providing a missing transverse momentum measurement. At high energy the mass of most particles is negligible and missing transverse momentum and missing transverse energy become interchangeable.

⁷Pseudorapidity, $\eta = -\ln \tan \frac{\theta}{2}$ where $\cos \theta = \frac{p_z}{p}$, is the high energy ($p \gg m$) approximation to rapidity, $y = \frac{1}{2} \ln \frac{E+p_z}{E-p_z}$. Rapidity is a useful angular variable for hadronic collider physics since the shape of the rapidity distribution $\frac{dN}{dy}$ is invariant under a longitudinal boost.

The hadronic “Tile Calorimeter”, with an outer radius of 4.25 m extending ± 6.10 m longitudinally, is located at larger radii where the radiation levels are lower and the less expensive iron-scintillator technology is suitable. The Tile Calorimeter is separated into one large barrel and two extended barrel cylinders on either side.

The muon spectrometer, which measures the curvature of muon trajectories, surrounds the calorimetry system and consists of three stations of high-precision tracking chambers complemented by fast trigger chambers. The light and open structure of the air-core toroid system minimizes multiple scattering effects while providing strong bending power over a large field volume.

More information on the ATLAS detector can be found in Ref. [4], [5].

This paper focuses on the Hadronic Endcap calorimeter.

4 Particles Interactions and Showers in Matter

The interactions of particles with matter are briefly reviewed in this section. Electrons and photons are discussed first, followed by muons and then hadrons.

4.1 Electrons and Photons

The dominant interaction for high energy electrons above $\simeq 10$ MeV in dense matter is Bremsstrahlung (Figure 3a), the emission of a photon in the presence of an atomic nucleus. Photons above about 10 MeV predominantly interact by pair production (Figure 3b), the creation of an e^+e^- pair in the presence of the electromagnetic field of a nucleus or electron. When a sufficiently high energy electron or photon is incident on a dense medium, an electromagnetic cascade is initiated with electrons producing photons by Bremsstrahlung and photons pair producing to form an electron and positron. We refer to this cascade as an electromagnetic shower.

In the context of electromagnetic showers, it is useful to measure material thicknesses in units of radiation length X_o , the mean distance over which a high energy electron’s energy is reduced to $1/e$ of its initial value by Bremsstrahlung. In copper $X_o = 1.43$ cm and in liquid argon $X_o = 14$ cm [6]. The characteristic length for pair production by photons differs slightly. The photon attenuation length, approximately related to the radiation length by $X_p \simeq \frac{9}{7}X_o$, is the distance over which the intensity of a photon beam is reduced by $1/e$.

Eventually a high energy e^\pm will lose enough energy that Bremsstrahlung will no longer be the dominant interaction and ionization will take over. The critical energy, approximated by $E_c = \frac{800 \text{ MeV}}{Z+1.2}$ [6], is the energy at which losses due to ionization equal the losses due to Bremsstrahlung. Below E_c electrons dissipate their energy by ionization and excitation and the electromagnetic cascade stops.

The transverse development of an electromagnetic shower scales as the Molière radius $R_M = 21 \text{ MeV} \frac{X_o}{E_c}$. Approximately 90% (99%) of the shower energy is deposited inside a cylinder of radius R_M ($3.5R_M$). For copper, $R_M \simeq 1.13$ cm.

The physics of electromagnetic showers is well understood and can be reliably simulated by Monte Carlo methods [7].

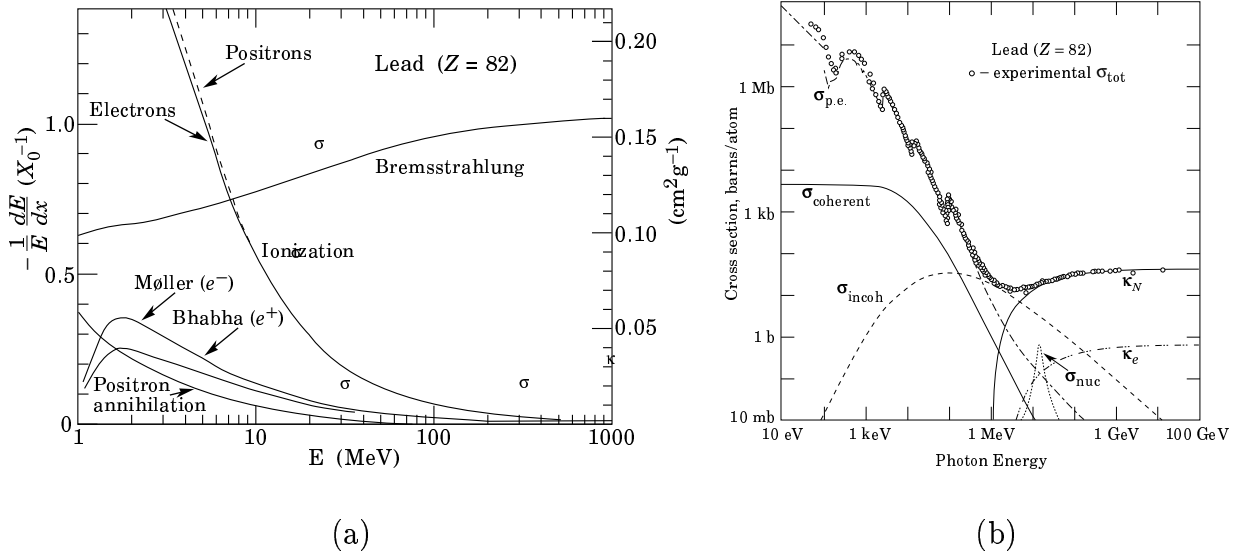


Figure 3: Fractional energy loss per radiation length in lead as a function of electron or positron energy (a). Photon total cross sections as a function of energy in lead, showing the contributions of different processes (b) where κ_N is pair production in a nuclear field, σ_{incoh} is Compton scattering off an electron, $\sigma_{\text{p.e.}}$ is the photo-electric effect, and the other notation is given in Ref. [6, P. 153].

4.2 Muons

The Bremsstrahlung cross section is proportional to the inverse of the incident particle mass squared (m^{-2}). This results in the “critical energy” for muons occurring at several hundred GeV. As a consequence, the majority of muons produced at high energy physics experiments including the LHC will lose energy by ionization. Ionization energy losses are well described by the Bethe-Bloch equation

$$-\frac{dE}{dx} = \frac{4\pi Z N_a z^2 e^4}{m_e c^2 A \beta^2} \left[\frac{1}{2} \ln \frac{2m_e c^2 \beta^2 \gamma^2 T_{\text{max}}}{I^2} - \beta^2 - \frac{\delta}{2} \right] \quad (1)$$

where the notation is as defined in [6, Equation 23.1]. To first order Equation 1 depends only on the incident particle $\beta\gamma$ (i.e.: on its velocity) and is independent of its mass. The $\frac{dE}{dx}$ curve has a minimum at $\beta\gamma \simeq 3$, and rises very slowly above the minimum. Particles which deposit the minimum ionization energy are labeled *minimum ionizing particles* (mip). The ionization energy deposited by a minimum ionizing particle in copper is $12.6 \frac{\text{MeV}}{\text{cm}}$.

High energy muons, occupying the “region of logarithmic rise” above the minimum in the $\frac{dE}{dx}$ curve, deposit very little energy as they pass through dense material and are able to escape most particle detectors without being absorbed. For example, a 120 GeV muon deposits only about 3 GeV of ionization energy after traversing 2 m of copper.

4.3 Hadrons

The interactions of hadrons (strongly interacting particles such as baryons and mesons) in matter are considerably more complicated than the electromagnetic case. More than 300 different reactions contribute to the total cross section ⁸ [8].

The *spallation model* describes hadronic showers phenomenologically. The hadronic cascade development is described by the spallation (break up) of nuclei by fast hadrons with the production of secondary particles. Fast hadrons enter a nucleus of the matter and scatter off a single nucleon, transferring some portion of energy to it. The scattered nucleon transfers energy to the nucleus and the process continues such that a “fast intra-nuclear cascade” develops. Additional hadrons (mostly pions) are produced and contribute to the cascade if sufficient energy transfer occurs.

Following this initial fast phase of shower particle production, a slow phase of nuclear de-excitation occurs. Nuclei are returned to their ground state by evaporating nucleons and by the spallation of larger nuclear fragments. *Photo-emission* (the emission of low energy photons) occurs at the last stages of the de-excitation.

It is difficult to detect energy from the slow phase and the detector signal is dominated by the fast phase. Due to the undetected slow phase energy, labeled *invisible energy*, it is difficult to model hadronic showers in computer simulations. Though several hadronic shower Monte Carlo simulation packages exist, no single package can be described as the standard in high energy physics.

Approximately a third of pions produced in each hadron collision are neutral and decay almost instantaneously to a pair of photons. Thus the cascade initiated by π^0 's proceeds electromagnetically and each hadronic shower has an electromagnetic fractional component F_{π^0} . Wigmans [8] has parameterized the electromagnetic fractional component as

$$F_{\pi^0} = k \ln E(\text{GeV}) \quad (2)$$

where $k \simeq 0.11$. More recently Groom [9] has proposed the parameterization

$$F_{\pi^0} = 1 - \left(\frac{E}{E_{\text{scale}}} \right)^{m-1} \quad (3)$$

where E_{scale} is the energy at which π^0 production becomes important (commonly taken as 1 GeV) and m is related to the multiplicity of high-energy secondaries in a single hadron-nucleus collision (typically $0.8 < m < 0.9$).

The flow of energy from hadronic showers to the electromagnetic sector is one way- it is not reconverted to hadronic forms. The total transfer fraction F_{π^0} increases with incident particle energy (since the number of high energy collisions in the cascade increases) and event by event fluctuations in F_{π^0} are large.

In general electromagnetic and hadronic⁹ components of a shower are converted to electrical signals in a detector with different efficiencies. The ratio of conversion efficiencies is

⁸The figure 300 includes only contributions with probability $> 0.1\%$, though none of these reactions contributes with more than 2% to the total cross section.

⁹Hence-forth the term “hadronic component” will exclude the electromagnetic component from π^0 's in a hadron shower.

referred to as the intrinsic $\frac{e}{h}$. For a *compensating calorimeter* $\frac{e}{h} = 1$, but typically $\frac{e}{h}$ is greater than 1 (due to the “invisible” slow component of a hadron shower). This results in a hadron response which is nonlinear and therefore the ratio of electron to hadron response $\frac{e}{\pi}$ is energy dependent.

The scale appropriate for hadronic showers is the nuclear interaction length $\lambda_I \simeq 35 \frac{g}{\text{cm}^2} A^{\frac{1}{3}}$ [6], the mean free path of high energy neutrons between two inelastic interactions in matter. Approximately 95% of the hadronic shower energy is contained in a cylinder of radius λ_I independent of energy [10]. For copper $\lambda_I = 15.1$ cm and for liquid argon $\lambda_I = 97.3$ cm.

5 Sampling Calorimetry

As high energy particle physics colliders achieve ever higher energies, the role of calorimetry becomes increasingly important compared to other subdetector types since the size of calorimeter necessary to measure the energy of a particle scales like the logarithm of the particle energy, whereas the size of magnetic spectrometers scale like the square root of particle energy.

Calorimeters are total absorption detectors used in high energy physics collider experiments to measure the energy and direction (E, \vec{p}) of particles and jets as well as for particle identification and triggering. The energy of an incident particle is measured by absorbing it as completely as possible and converting the energy deposited into some type of signal based on charge or light collection. Whereas most other subdetectors rely on magnetic fields and can only detect charged particles, calorimeters are able to detect neutral particles. Segmentation of calorimeters allows for the determination of the particle direction. Particle identification is achieved based on the spatial distribution of particle showers since electromagnetic showers (initiated by electrons and photons) are dense and localized, whereas hadronic showers (initiated by baryons and mesons) are widely spread, and muons typically do not shower.

A calorimeter may be homogeneous and fully active such as lead glass and sodium iodide scintillation detectors wherein photons are produced in direct proportion to the energy deposited in the medium. These calorimeters are called total absorption calorimeters. Another class of calorimeters, called *sampling calorimeters*, periodically sample the development of a shower initiated by an incident particle. This is achieved by interspersing active layers (such as an ionizing liquid/gas or scintillating medium) between layers of high density absorber material (typically lead, uranium, iron, copper or tungsten).

A signal is produced by collecting charge or light in the active medium of the calorimeter. If we define the sum of all the charged particle tracks in a shower as the *total track length* T and assume there is no cutoff on the minimum kinetic energy of a particle that can be detected in the calorimeter (for an expression for T with non-zero kinetic energy cutoff see [10, Eqn. 6]), then

$$T(X_o) = \frac{E_o}{E_c} \quad (4)$$

where E_o is the incident particle energy. Since the total track length (an indirectly measurable quantity in a calorimeter) is proportional to E_o , it is possible to reconstruct the incident

particle energy by measuring T .

For the case of ionization media, a sufficiently energetic charged particle deposits an amount of ionization charge proportional to the distance traversed in the media. If we assume that all of the charged tracks traverse the ionization media perpendicularly, then by collecting the charge from the active media an estimate can be made of the total track length and hence of the incident particle energy.

The ratio of energy E_{act} deposited in the active layers of a calorimeter to the total energy deposited anywhere in the calorimeter E_{tot} is called the *sampling fraction* S . For electrons and photons S is generally found to be independent of the incoming particle energy. This feature of electromagnetic showers is referred to as *signal linearity*.

The sampling fraction is often evaluated for mip signals. By expressing the energy loss $\frac{dE}{dx}$ of a charged particle traversing a distance d as $\Delta E = \frac{dE}{dx} \cdot d$ then the mip sampling fraction may be written

$$S_{\text{mip}} = \frac{E_{\text{act}}}{E_{\text{tot}}} = \frac{\frac{dE}{dx} \Big|_{\text{act}}^{\text{mip}} \cdot d_{\text{act}}}{\frac{dE}{dx} \Big|_{\text{act}}^{\text{mip}} \cdot d_{\text{act}} + \frac{dE}{dx} \Big|_{\text{abs}}^{\text{mip}} \cdot d_{\text{abs}}} \quad (5)$$

where the subscripts “act” and “abs” refer to the active and absorber layers of the calorimeter respectively¹⁰.

5.1 Hadronic Calorimetry

There are two main types of sampling calorimeters optimized for the detection of either electromagnetic or hadronic showers. The scale of electromagnetic cascades, governed by the radiation length X_o , is considerably smaller than that of hadronic showers, governed by the interaction length λ_I . As such, hadron calorimeters must be significantly larger than electromagnetic calorimeters and the segmentation of hadron calorimeters need not be as fine.

5.1.1 Response

A calorimeter’s response is the ratio of signal to incident particle beam energy. For the case of electromagnetic cascades, the track length is proportional to the beam energy and linear response is achievable.

This holds for the fraction F_{π^o} of a hadron shower which is electromagnetic. The purely hadronic component deposits much of its energy as invisible energy. We may express the energy deposited anywhere in the calorimeter E_{dep} for hadronic showers as

$$E_{\text{dep}} = E_{\text{dep}}^{\pi^o} + E_{\text{dep}}^{\text{ion}} + E_{\text{dep}}^{\text{inv}} \quad (6)$$

where $E_{\text{dep}}^{\pi^o}$ is the electromagnetic component originating from neutral pions decaying to photons, $E_{\text{dep}}^{\text{ion}}$ is the energy deposited by ionizing particles (mainly π^\pm), and $E_{\text{dep}}^{\text{inv}}$ is invisible deposited energy.

¹⁰The sampling fraction as defined is intrinsic to the geometry of the calorimeter and is independent of the readout. Confusion exists in the literature between this “intrinsic” sampling fraction and the “measured” sampling fraction which includes charge collection, integration, and readout effects.

The fraction of the total energy in each of these components is energy dependent. Since for noncompensating ($\frac{\epsilon}{h} \neq 1$) calorimeters the response to each component is different, the overall response to hadrons is in general energy dependent (nonlinear). The response to hadrons (for $\frac{\epsilon}{h} > 1$ which is commonly the case) increases with energy since the fractional contribution of the electromagnetic component $E_{\text{dep}}^{\pi^0}$ increases with energy (see Equations 2&3).

5.1.2 Energy Resolution

The energy resolution is a measure of how well an incident particle's energy can be reconstructed. Assuming the reconstructed energy for a fixed particle beam energy E_o has a Gaussian distribution, the energy resolution is $\frac{\sigma}{E}$ where σ is the distribution width and E is the mean. The energy resolution is energy dependent and is normally ¹¹ parameterized as

$$\frac{\sigma}{E} = \frac{A}{\sqrt{E_o}} \oplus B \oplus \frac{C}{E} \quad (7)$$

where \oplus indicates the terms are added in quadrature.

The *sampling term*, proportional to A , normally dominates and reflects the statistical nature of the shower cascade development. Since the average number of secondary particles $\langle N \rangle$ is proportional to the incident energy E_o , the uncertainty in the reconstruction of the particle energy is determined by fluctuations in N . As such, the energy resolution improves with higher energy $\frac{1}{\sqrt{\langle N \rangle}} \sim \frac{1}{\sqrt{E_o}}$.

The *constant term* B reflects calorimeter nonuniformities, calibration errors, pedestal fluctuations, incomplete shower containment, and the degree of noncompensation ($\frac{\epsilon}{h} \neq 1$) of the calorimeter.

The *noise term*, proportional to C , arises primarily from noise in the electronics chain. Since the contribution of the noise to the signal distribution width is approximately constant, the noise term in the resolution parameterization is inversely proportional to the signal amplitude irrespective of the incident particle energy. For the case of electromagnetic calorimeters E and E_o are linearly related and the noise term is often written $\frac{C}{E_o}$. In general this is not true for hadron calorimeters and the noise term scales as $\frac{1}{E}$.

The noise term dominates at low energy. At high energy the constant term dominates and the resolution ceases to improve with energy. At LHC energies the constant term can play an important role in overall calorimetry performance, and has to be kept small.

The energy resolution of a hadron calorimeter is in general much worse than can be achieved for electromagnetic shower detection. The effects associated with the excitation of the absorbed nuclei (which contribute to the slow phase and invisible energy of the hadronic shower) and the wide variety of possible interaction processes are considered responsible for this [8].

¹¹Other parameterizations exist, including a linear sum of the first two terms in equation 7 and a four component parameterization proposed in [11].

6 The ATLAS Hadronic Endcap

The Hadronic Endcap Calorimeter (HEC) is a liquid argon sampling calorimeter with copper absorbers and is designed to provide coverage for hadronic showers in the forward region ($1.5 < |\eta| < 3.2$) of the ATLAS detector. It will be located in the endcap cryostats at either end of the ATLAS detector (Figure 1).

The construction ¹² of the first HEC modules built to the final ATLAS specifications was completed in spring 1998. Unlike previous prototypes ¹³, these modules contain 10 interaction lengths affecting near full longitudinal containment of hadronic showers.

One full ATLAS HEC will consist of 32 pie-shaped modules as shown in Figure 4. The readout segmentation will be $2\pi/64$ in azimuthal angle ϕ and 0.05-0.1 in pseudorapidity η . The two beam test modules consist of four ϕ segments (2 per module) totaling 1/16 of one endcap.

Longitudinally the calorimeter is divided into three readout segments. The first segment ($z = 1$) is about $1.3\lambda_I$ in depth and consists of 8 liquid argon (LAr) gaps each separated by 2.5 cm of copper. The second segment ($z = 2$), about $2.7\lambda_I$ in depth, consists of 16 LAr gaps also separated by 2.5 cm of copper. The third segment ($z = 3$) consists of 16 gaps each separated by 5 cm of copper and is about $5.3\lambda_I$ in depth.

The mip sampling fractions in the front wheel and back wheel are $S_{\text{mip}}^{\text{front}} \simeq 0.051$ and $S_{\text{mip}}^{\text{back}} \simeq 0.026$ respectively. The change in sampling fraction in the third segment (second wheel) necessitates the application of a factor of two relative to the first two segments (front wheel) when reconstructing the energy deposited in this layer.

6.1 Electrode Structure

A schematic diagram of the HEC electrode structure in the 8.5 mm gaps is presented in Figure 5. Honeycomb layers maintain the 1.735 mm spacing of the 4 LAr subgaps between the three readout boards and the grounded copper plates. The transverse readout segmentation is defined by the pad structure which is etched on these boards.

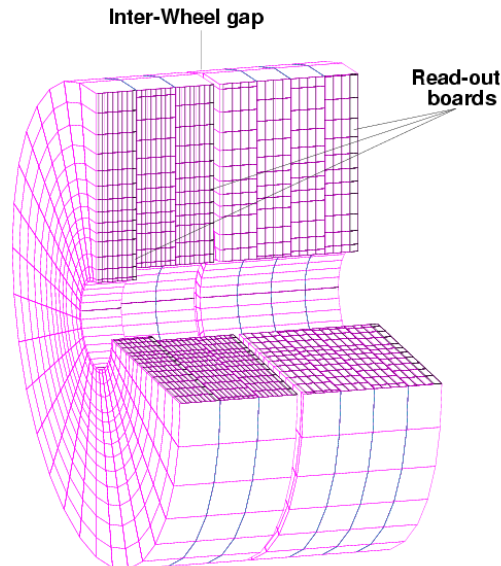


Figure 4: Three dimensional view of one ATLAS HEC including front and back wheels. Read-out boards in two of the 40 LAr gaps are indicated. The total depth of the HEC is about 2 m.

¹²One half of the modules was constructed in Russia and assembled in Germany, while the other half was constructed and assembled entirely in Canada at the TRIUMF laboratory in Vancouver. TRIUMF personnel based at the University of Victoria, Terry Hodges and Roy Langstaff, form the engineer team in charge of

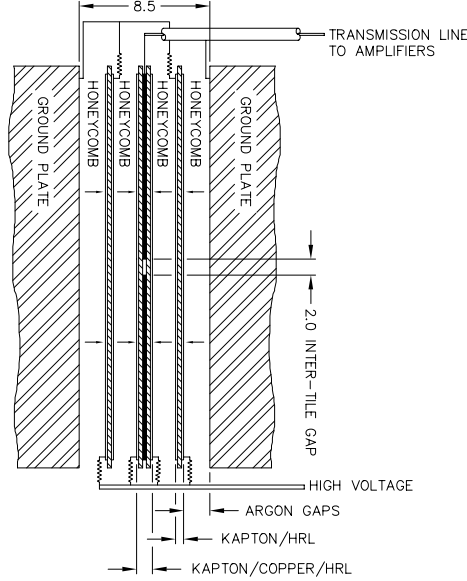


Figure 5: Subgap structure within each LAr gap [4, Fig. 8-4]. The distance between copper ground plates is 8.5 mm.

The two outer boards form an electrostatic transformer (EST) structure which reduces the high voltage required to achieve the large electric field ($\sim 10000\text{V/cm}$) necessary to accelerate the ionization charge (electrons). The total electron drift distance is reduced as well, ensuring no ion build-up problems arise in the high luminosity environment of the LHC.

The beam test modules are identical with the exception of the high resistive coating which implements the high voltage distribution within the gaps and combines the functions of the charge collection anode with that of the high voltage blocking capacitor. One module uses a Carbon Loaded Paint (CLP) as a resistive coating, while the other uses a Carbon Loaded Kapton (CLK) resistive coating. The performance of the two coatings is similar, but cost and construction considerations dictate that the CLK resistive coating will be employed in all modules for the final ATLAS design.

6.2 Calibration

In order to obtain a relationship between the charge collected on the readout boards and the electronic signal, each readout cell is calibrated individually with calibration pulses. The pulses are produced by external calibration generators and are distributed to all signal pad groups by a network of coaxial cables and printed strip lines.

The calibration current is ramped across the range of signal output (in analog to digital converter counts, ADC's) and a fit is performed to a 3rd-order polynomial.

the HEC design.

¹³Prototypes have been previously tested in particle beams at CERN [12].

Calibration constants are applied to the data off line and are found to improve the linearity of the response in the April 1998 beam test period [1].

6.3 LAr Temperature Considerations

The LAr density and electron drift speed v_d in the gaps are sensitive to temperature fluctuations. The signal has about $0.5\%K^{-1}$ sensitivity to temperature. Since fast signal shaping is necessary due to the high interaction rate of the LHC, the signal is directly proportional to v_d . This increases the total temperature dependence to $\sim 2\%K^{-1}$ [13]. As such, a uniform liquid temperature bath is required. A temperature difference smaller than 0.3 K within the cryostats housing the calorimetry is expected in the final ATLAS design.

During the beam test, the temperature of the LAr was constantly monitored at several points inside the cryostat. Typical temperature fluctuations over several experimental runs (several hours) are about ± 0.02 K and so the effect on the signal is expected to be small.

7 Beam Test Experimental Setup

The modules were installed in a cryostat in a beamline of the CERN Super Proton Synchrotron (SPS) and immersed in liquid argon at the standard operating temperature of 89.8 K. The LAr fills the gaps between the copper plate absorbers and forms the active layers of the calorimeter.

Though the Hadronic Endcap is constructed so as to provide a semi-pointing geometry in pseudorapidity, space constraints within the cryostat prevent the modules from being tilted such that beam particles are incident in a pointing manner (see Figure 6). Therefore a hadronic shower will deposit energy in a larger number of cells than it would in a pointing orientation, necessitating the use of larger clusters of cells and increasing the electronic noise contribution to the energy resolution.

In April 1998, electron, pion, and muon beam test data were recorded with incident energies of 20 to 180 GeV. Trigger counters and multi-wire proportional chambers installed in the beamline (see Figure 7) provide trigger and particle identification information and are described in Section 8.1.

7.1 High Voltage

During the April 1998 beam period, module 2 suffered from high voltage problems in its third readout segment, requiring 1 subgap in each of the first 8 gaps to be disconnected from high voltage, while one subgap in each of the second 8 gaps had its high voltage reduced by a factor of $\frac{1}{3}$. As will be shown in the sections to follow, the resolution of module 2 is recoverable by using simple multiplicative depth constants to offset the effective change in sampling fraction due to HV problems.

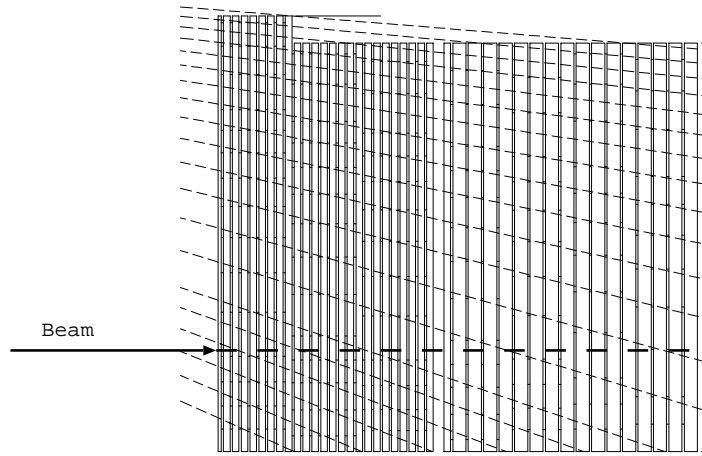


Figure 6: Orientation of the beam with respect to the calorimeter. The thick line represents the incident (non-pointing) particle beam. The thin dashed lines are drawn at constant pseudorapidity from the ATLAS interaction point, such that a particle traveling in a straight line from the vertex would follow this trajectory. The readout cells are positioned in a “semi-pointing” manner which follows these pseudorapidity lines in a stepped fashion.

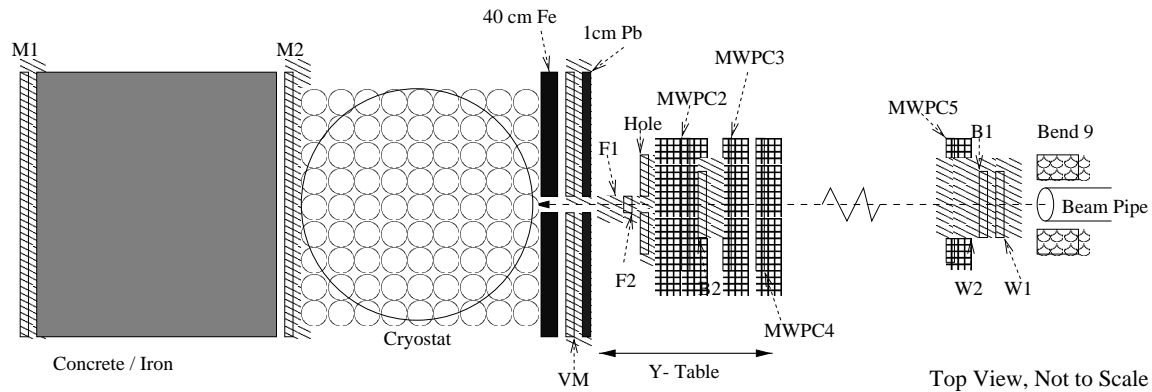


Figure 7: Setup of the HEC testbeam. The cryostat sits on a track which facilitates horizontal motion and a dipole magnet, labeled *Bend9*, can bend the particles in the vertical direction as they leave the beam-pipe. Descriptions of the trigger counters are provided in the text.

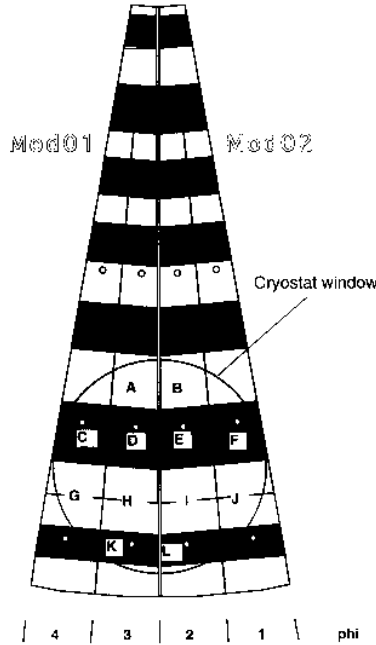


Figure 8: The geometric layout of impact positions D, E, H, & I on the front face of HEC modules. The cryostat window is about 50 cm in diameter. The center of the impact positions are separated by about 20 cm horizontally and about 15 cm vertically.

7.2 Data Samples

Energy scans at 4 impact positions for electron and pion beams are analyzed. Figure 8 shows the geometrical layout of the impact positions, labeled D, E, H, & I. Impact positions D & E (H & I) belong to different modules but are identical in every other way. Positions D & E differ from positions H & I in that they each contain a tie rod which holds the layers of the calorimeter in place.

Pion data were taken at beam energies of 20, 40, 60, 80, 100, 120, and 180 GeV, while electron data were taken at 20, 40, 60, 80, 100, and 119.1 GeV. The momentum spread for a given beam energy is typically of the order 0.1%. Each run consists of 6,000 to 10,000 events (including random triggers and physics events) with the exception of the 20 GeV pion runs which suffered from low rate and contain 1000 to 2000 events.

The total electron drift time in the HEC readout cells is about 400 ns. In the ATLAS environment, the 25 ns bunch crossing rate means that full charge integration signal shaping methods cannot be employed. The signal is “clipped” (integrating only a small fraction of the charge produced) and bipolar shaping is used. The signal is sampled every 25 ns and only 4 to 5 samples will be available for a given event.

In the beam test similar constraints are imposed on the signal reconstruction. The signal from each readout cell for each event is recorded every 25 ns (irrespective of the arrival time of an incident particle) for a total of 16 time slices. Figure 9 shows a typical signal shape. The

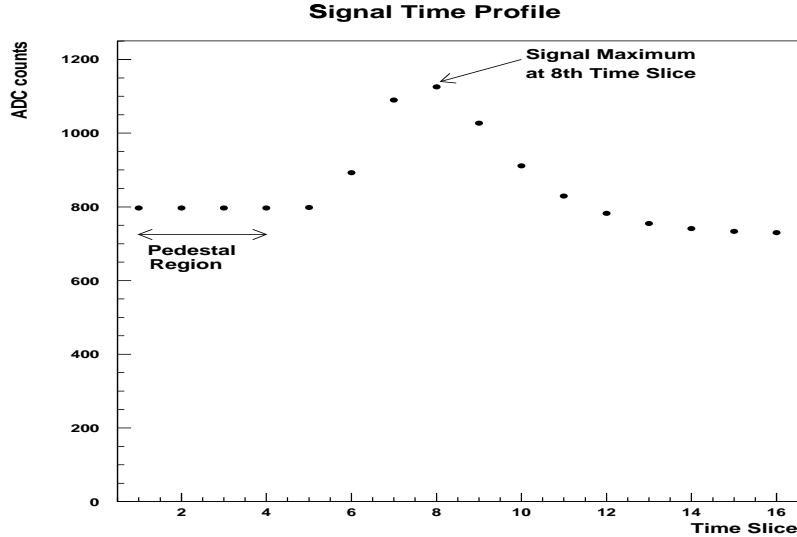


Figure 9: Sample signal time profile (average signal for 180 GeV pions, impact position D) showing the pedestal region (time slices 1-4) and the signal maximum which typically occurs at time slice 8. The time slices are separated by 25 ns.

first 4 time slices occur before the signal rise, while the signal maximum typically occurs in the 8th time slice. The energy deposited in each cell is reconstructed from the signal maximum which is determined from five time slices using the “digital filtering method”¹⁴. [14]. This method maximizes the signal to noise ratio by using the autocorrelation function of the time slices for the determination of the amplitude and time origin of the signal.

The pedestals for each cell are determined from the first four time slices averaged over all events within the run, as shown in Figure 9. On an event by event basis the average of the first 4 time slices is observed to be stable over the duration of a run. Over the course of physics data runs *random trigger* events were recorded. Pedestals calculated from these events, recorded when no physics signal was present in the calorimeter, are in agreement with the pedestals calculated from physics events, implying the pedestals are not rate dependent.

After pedestal subtraction, calibration coefficients (described in Section 6.2) are applied in order to express the signal in terms of the current in nA deposited in each cell.

8 Electron Energy Scans

The HEC is not optimized for the detection of electrons. In the ATLAS environment electromagnetic showers will rarely penetrate through the Electromagnetic Endcap to reach the HEC. The calorimeter’s performance to electromagnetic showers is nevertheless relevant

¹⁴For April 1998 data 4 cells did not have digital filtering coefficients. A simple cubic fit was used for these cells.

because of the electromagnetic content intrinsic to hadronic showers.

8.1 Event Selection

Events are recorded when simultaneous triggers are registered from $B1$, a scintillating detector upstream from the cryostat where the beam leaves the beam pipe, and $F1\&F2$, scintillating detectors which are oriented perpendicular to one another and effectively define the transverse size of the beam (a square about $2.5\text{ cm}\times 2.5\text{ cm}$) for triggered events. Refer to Figure 7 for the locations of the various detectors in the beam test setup. Events are vetoed for which a second event coincides with the first (pile-up) or a stray particle triggers either of the scintillating veto counters (VM or $hole$). Events with muon triggers, defined by coincidences in the two muon walls $M1\&M2$ located behind the cryostat and separated by a thick concrete absorber, are excluded.

Each event is further required to have at least one readout cell with a signal shape consistent with energy deposition in that cell. There are no requirements on the amplitude of the signal. The trigger and signal shape cuts are described in more detail in Ref. [1].

8.2 Energy Reconstruction

Having reconstructed the signal in each readout cell, the electron sample is isolated by applying trigger cuts and a signal shape cut. Total electron energies are then measured by summing the energy deposited in a predefined cluster and applying a global electromagnetic scale factor, α_{em} .

8.2.1 Clustering

The energy of the incident electrons is reconstructed by summing the individual energies deposited in a cluster of 3 cells. The cluster size and shape have been chosen so as to minimize the energy resolution. Each cluster consists of the impact cell and two cells in the second readout segment lying directly behind the impact cell. Figure 10 shows the clusters chosen for the 4 impact positions.

The energy deposited in each cluster is histogrammed and a Gaussian curve is fit to the data in a 2.5σ range about the mean for each run. Histograms and fits for a representative impact position (H) are shown in Figure 11.

8.2.2 Global Electromagnetic Scale, α_{em}

A single constant, α_{em} , is used to convert the energies from nA to GeV. This global electromagnetic scale is determined for each impact position from an average of $\frac{E_{0,i}}{\langle E_{cl,i} \rangle}$ weighted by the width of the reconstructed energy distributions, where $E_{0,i}$ is the i^{th} nominal beam energy in GeV and $\langle E_{cl,i} \rangle$ is the mean reconstructed energy for the i^{th} beam energy arrived at by fitting Gaussian curves to the energy distributions as described in Section 8.2.1.

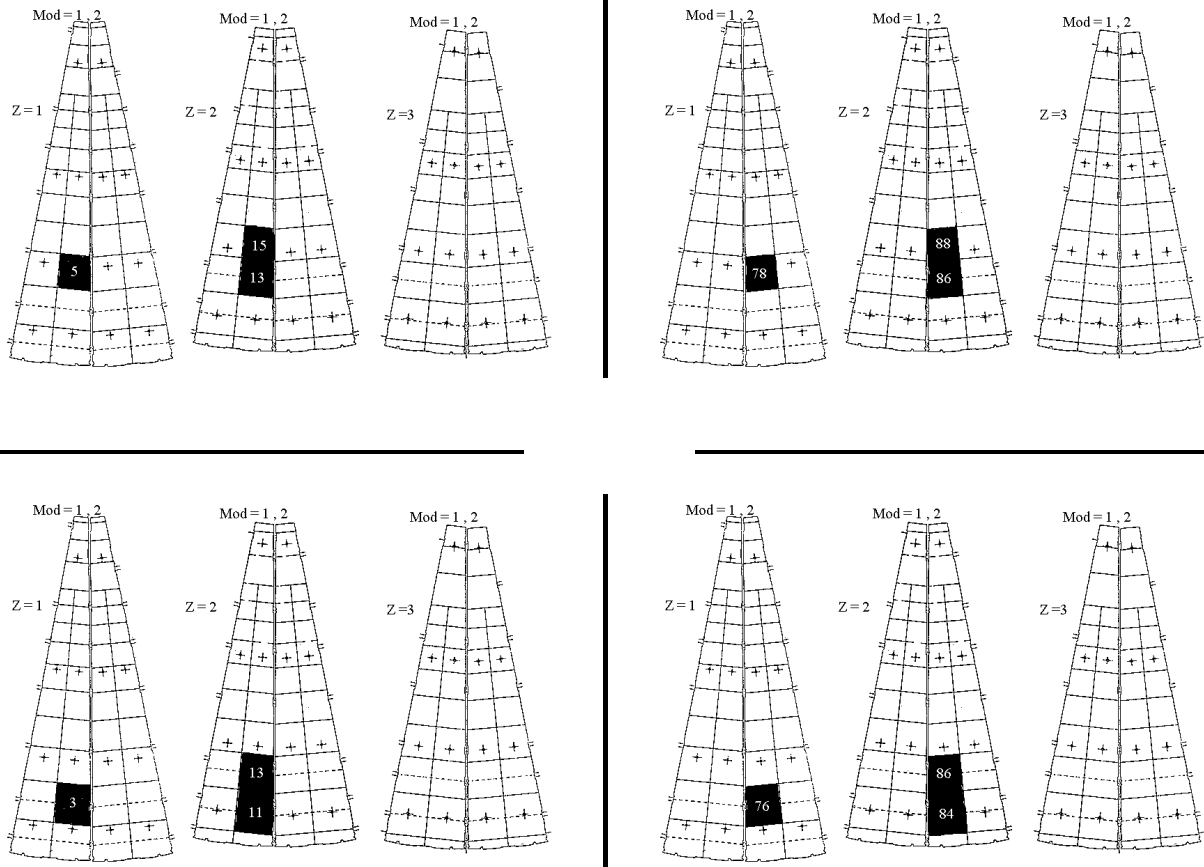


Figure 10: Map of 3 cell clusters used for electron data: impact positions D, E, I, H (clockwise from top left). The numbers in white refer to the readout cell channel number and are not relevant to this paper.

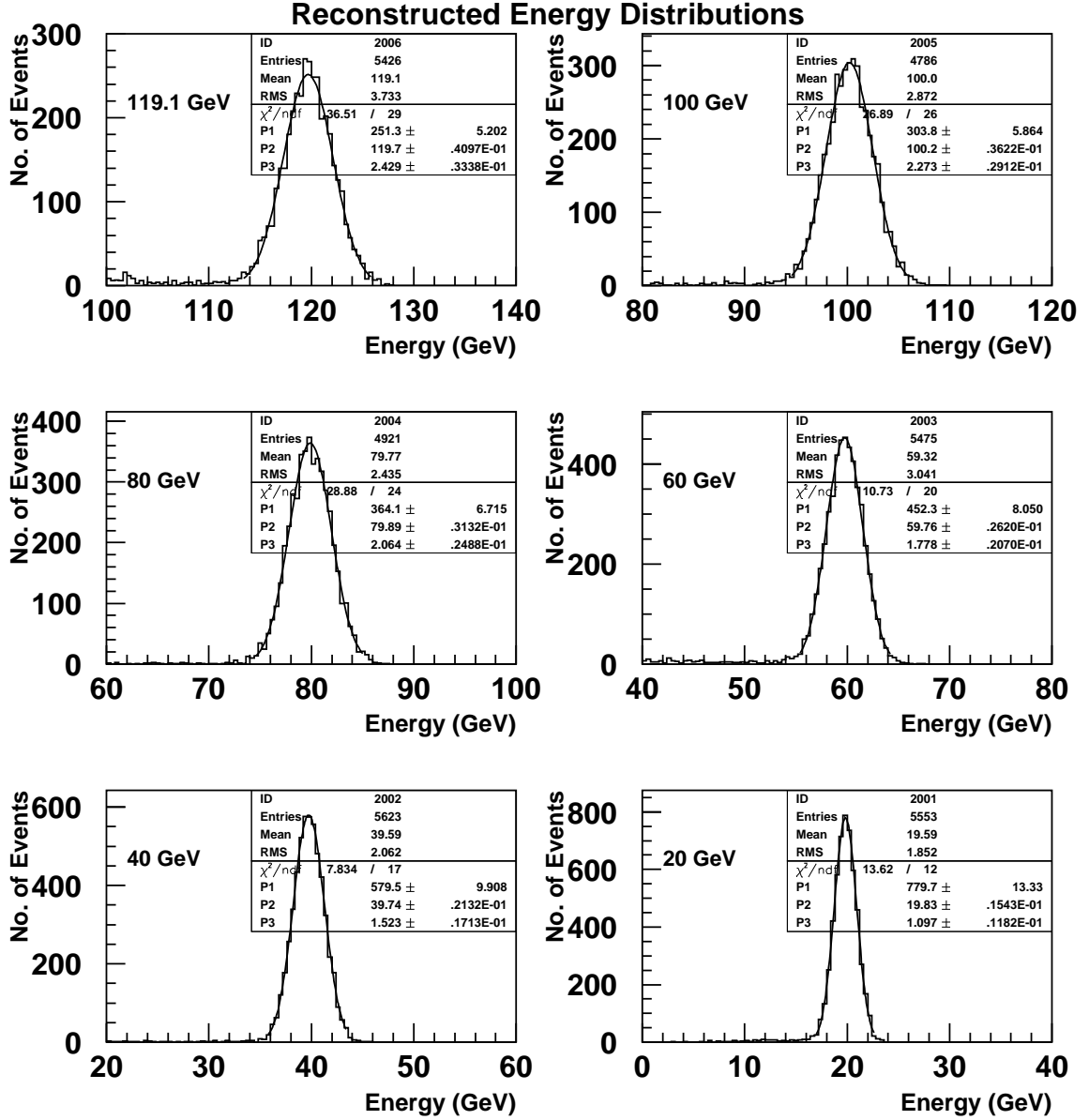


Figure 11: Electron cluster energy distribution for a typical impact point(H) for beam energies 119.1, 100, 80, 60, 40 and 20 GeV.

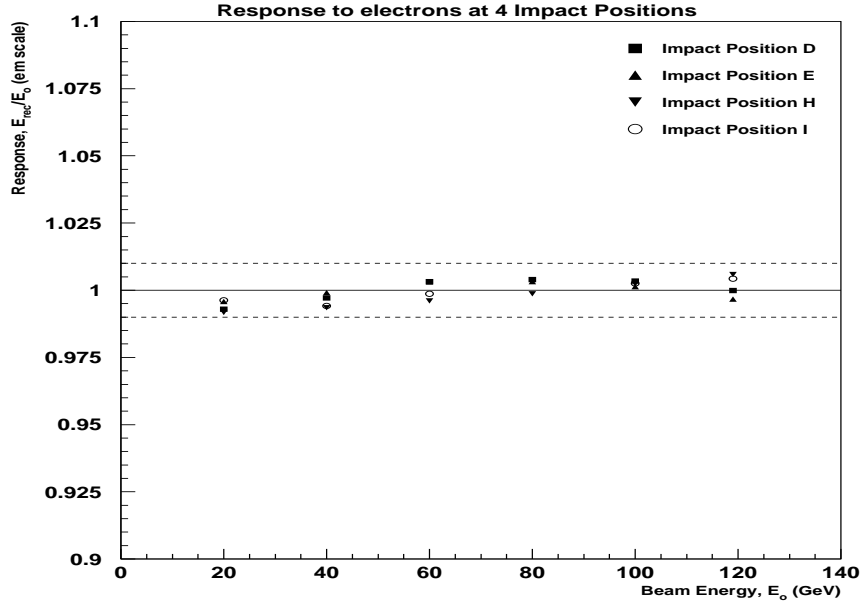


Figure 12: Electron response of calorimeter vs. beam energy.

The global electromagnetic scale is found to be similar at all impact points. The average over all 4 impact positions is:

$$\alpha_{em} = 3.41 \text{ GeV}/\mu\text{A}. \quad (8)$$

8.3 Response

By applying α_{em} to the fit mean energy for each run, a response curve is obtained, Figure 12. The response is linear to within 1% over all impact positions. The response curve is re-evaluated without the use of the hardware calibration described in section 6.2 and it is found that the response linearity is improved by the hardware calibration.

8.4 Resolution

The energy resolution σ/E is plotted versus the beam energy in Figure 13. The resolution of the calorimeter is parameterized according to Equation 7. The results of the fit for each impact position with all three parameters left free are:

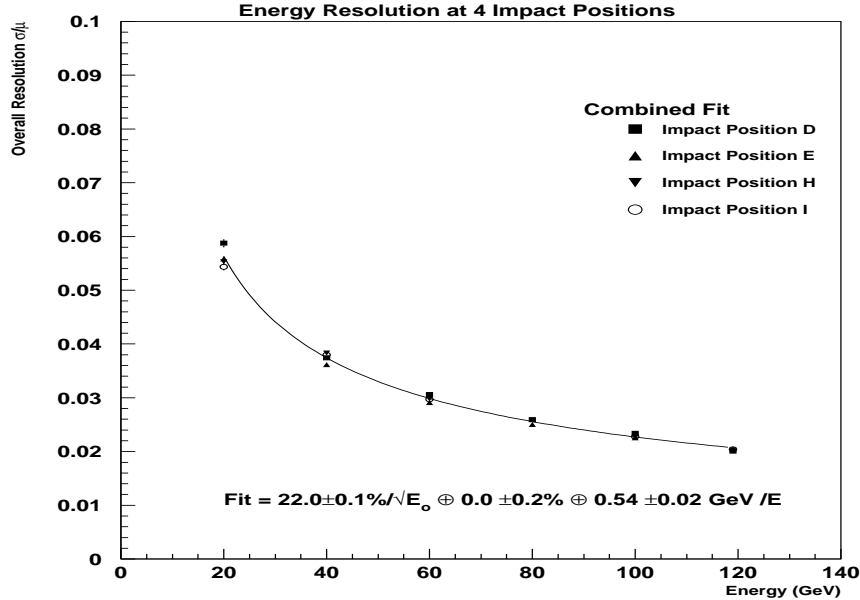


Figure 13: Electron energy resolution with 3 free parameters.

Position	A(%GeV ^{1/2})	B(%)	C(GeV)	χ^2/ndf
Module 1				
D	20.6 ± 0.5	0.7 ± 0.1	0.69 ± 0.04	6.5
H	22.1 ± 0.2	0.0 ± 0.3	0.52 ± 0.04	3.0
Module 2				
E	20.0 ± 0.9	0.8 ± 0.2	0.65 ± 0.05	0.3
I	22.1 ± 0.2	0.0 ± 0.3	0.49 ± 0.04	3.0

The results are consistent over all impact positions. A combined fit produces the following result:

$$\frac{\sigma}{E} = \frac{22.0 \pm 0.01\%}{\sqrt{E_0}} \oplus 0.0 \pm 0.2\% \oplus \frac{0.54 \pm 0.02}{E}, \quad \frac{\chi^2}{\text{ndf}} = 3.3 \quad (9)$$

where E_0 is expressed in GeV.

The noise has been measured with random trigger events of two types: inside the beam spill and between beam spills. The noise measured from random trigger events of both types is consistent with the noise terms from the fits. This indicates the noise is rate independent.

9 Electron to Muon Response Ratio

During the April 1998 beam test period, muon data runs were performed at a single energy only, 120 GeV. Muon events are selected using the same criteria as for electrons (Section 8.1) with the exception that only events satisfying the muon trigger are accepted. The energy is

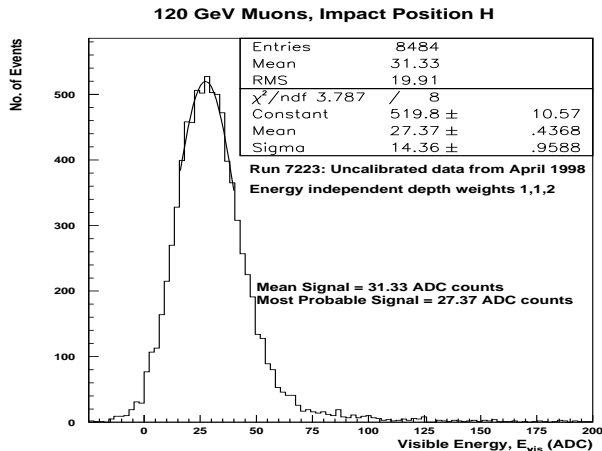


Figure 14: A typical 120 GeV muon energy distribution. The most probable energy is extracted from a Gaussian fit to a limited range about the peak.

reconstructed using a 6 cell cluster which includes all cells intersected by a straight line drawn from the beam-pipe through the HEC. “Simple depth constants” (described in Section 10.2) are employed to give an effectively constant sampling fraction.

A typical 120 GeV muon energy distribution is shown in Figure 14, and is seen to exhibit the expected Vavilov shape. The mean energy of such a distribution is sensitive to small fluctuations in the high energy tail, and so is difficult to measure. For this reason the most probable energy is chosen to characterize the distribution and is extracted using a Gaussian fit to a limited range about the peak.

In order to evaluate the electron to muon response ratio ($\frac{e}{\mu}$), it is necessary to know the total amount of energy the muons deposit anywhere in the calorimeter E_{dep}^{μ} . Lacking a detector behind the HEC to measure the momentum of outgoing muons, there was no means of performing this measurement experimentally during the beam test period. Instead, the total deposited energy is estimated from Monte Carlo simulation, $E_{\text{MC,dep}}^{\mu}$. The electron to muon response ratio may be expressed as

$$\frac{e}{\mu} = \frac{\frac{E_{\text{vis}}^e}{E_{\text{dep}}^e}}{\frac{E_{\text{vis}}^{\mu}}{E_{\text{MC,dep}}^{\mu}}} . \quad (10)$$

Full containment of the electron shower is ensured by employing a large cluster of 40 readout cells to determine E_{vis}^e . In this case, the electron beam energy E_0^e is a good approximation for E_{dep}^e .

Using the data from Figure 14 and the Monte Carlo prediction [16] $E_{\text{MC,dep}}^{\mu}|_{120\text{GeV}} = 2.73 \text{ GeV}$, the electron to muon response ratio is evaluated as

$$\frac{e}{\mu_{120\text{GeV}}} = 0.96 \pm 0.03 . \quad (11)$$

An estimate for the electron to mip response ratio can be made by evolving the muon energy down to mip energies using the method outline in [15], wherein the ratio is approximated by

$$\frac{e}{mip} = \frac{E_{\text{vis}}^e}{E_{\text{dep}}^e} \times \frac{E_{\text{Th,dep}}^{\text{mip}}}{E_{\text{vis}}^{\mu, 120\text{GeV}} \times \frac{E_{\text{Th,vis}}^{\text{mip}}}{E_{\text{MC,vis}}^{\mu, 120\text{GeV}}}}. \quad (12)$$

The $\frac{e}{mip}$ ratio using Equation 12 is 0.83 which agrees well with a calculation of $\frac{e}{mip}$ with Monte Carlo data used for the electron response and the mip response calculated from the Bethe-Bloch equation, $\frac{e}{mip}|_{\text{Th+MC}} = 0.82$.

10 Pion Energy Scans

10.1 Pion Sample

In order to remove impurities in the pion sample (eg. muons), several trigger cuts are used. These cuts have been described in detail for the electron analysis (Section 8.1) and include a physics trigger requirement, a muon veto, and a signal shape cut. The number of pion events satisfying these cuts ranges from approximately 4000 to 9500 for the 40 to 180 GeV runs, and 350 to 450 events for the 20 GeV runs. The residual contamination in the pion sample is small and has a negligible effect on the analysis.

The performance of the hadronic endcap calorimeter is evaluated using simple depth constants. These constants are not designed to optimize resolution, rather they are intended to provide a constant sampling fraction in the three readout segments of the calorimeter. This is necessary due to the increase in thickness in copper plates in the third calorimeter readout. This change in copper thickness requires the application of a factor of two to the readout of the rear compartment. A small modification of this scheme is introduced for module 2 in order to correct a high voltage problem in the rear of that module. Since only 3/4 of the sub-gaps were functioning in the first half of the readout segment¹⁵ a corrective factor of 4/3 is applied to the third readout segment of this module (depth constant is 2.67 times the first two constants).

10.2 Energy Reconstruction

For the purpose of evaluating the intrinsic performance of the calorimeter, it is necessary to use clusters that achieve near full containment of hadronic showers. For this reason 39 cell clusters¹⁶ are used to reconstruct pion energy. A sample cluster for impact position H is shown in Figure 15.

The signal in each cell of the cluster is summed (using the appropriate simple depth

¹⁵The second half of the readout segment contains little energy and so is ignored in this assumption.

¹⁶The 39 cell clusters are chosen on a geometrical basis, though in general the chosen cells are those with the highest mean energy.

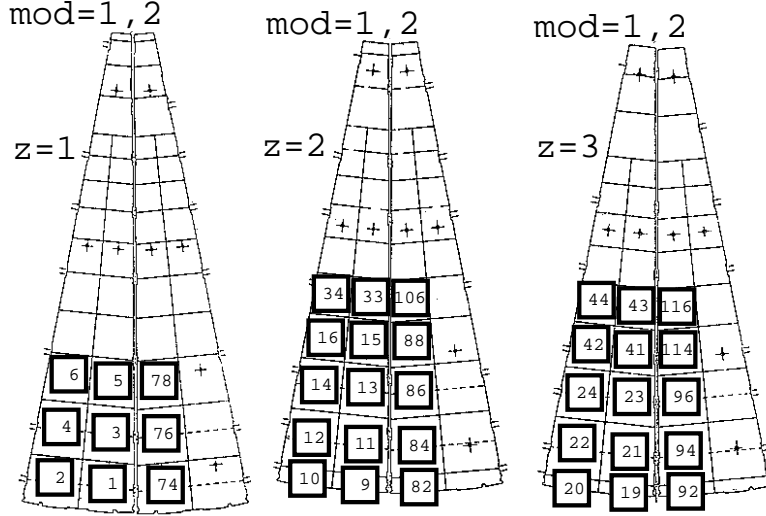


Figure 15: Map of 39 cell cluster used for pion data: impact position H. The numbers in the small boxes refer to the readout cell channel number and are not relevant to this paper.

constant) to reconstruct the particle energy for each event:

$$E_{cl} = \sum_z (c_z^{\text{mod1}} E_{cl}^{z, \text{mod1}}(nA) + c_z^{\text{mod2}} E_{cl}^{z, \text{mod2}}(nA)) \quad (13)$$

where $E_{cl}^{z, \text{mod1}}(nA)$ and $E_{cl}^{z, \text{mod2}}(nA)$ are the summed signals in readout segment z of modules 1 and 2 respectively and the simple depth constants are tabulated:

readout segment	c_z^{mod1}	c_z^{mod2}
1	1	1
2	1	1
3	2	2.67

The hadronic scale constant (α_{had}) needed to convert E_{cl} to GeV is found in the same manner as for the electron case:

$$\alpha_{\text{had}} = 4.1 \text{ GeV}/\mu A' \quad (14)$$

where the prime is included to remind the reader that α_{had} is applied *after* the simple depth constants, and hence is not a direct conversion from nA to GeV.

The results of this energy reconstruction are shown in Figures 16 and 17. These distributions show the expected Gaussian shape.

10.3 Electronic Noise Evaluation

In order to evaluate the electronic noise in each cluster, the reconstructed energy of the cluster (including simple depth constants) is measured for random trigger events. The distributions obtained from this method are centered on zero and the rms deviation is used

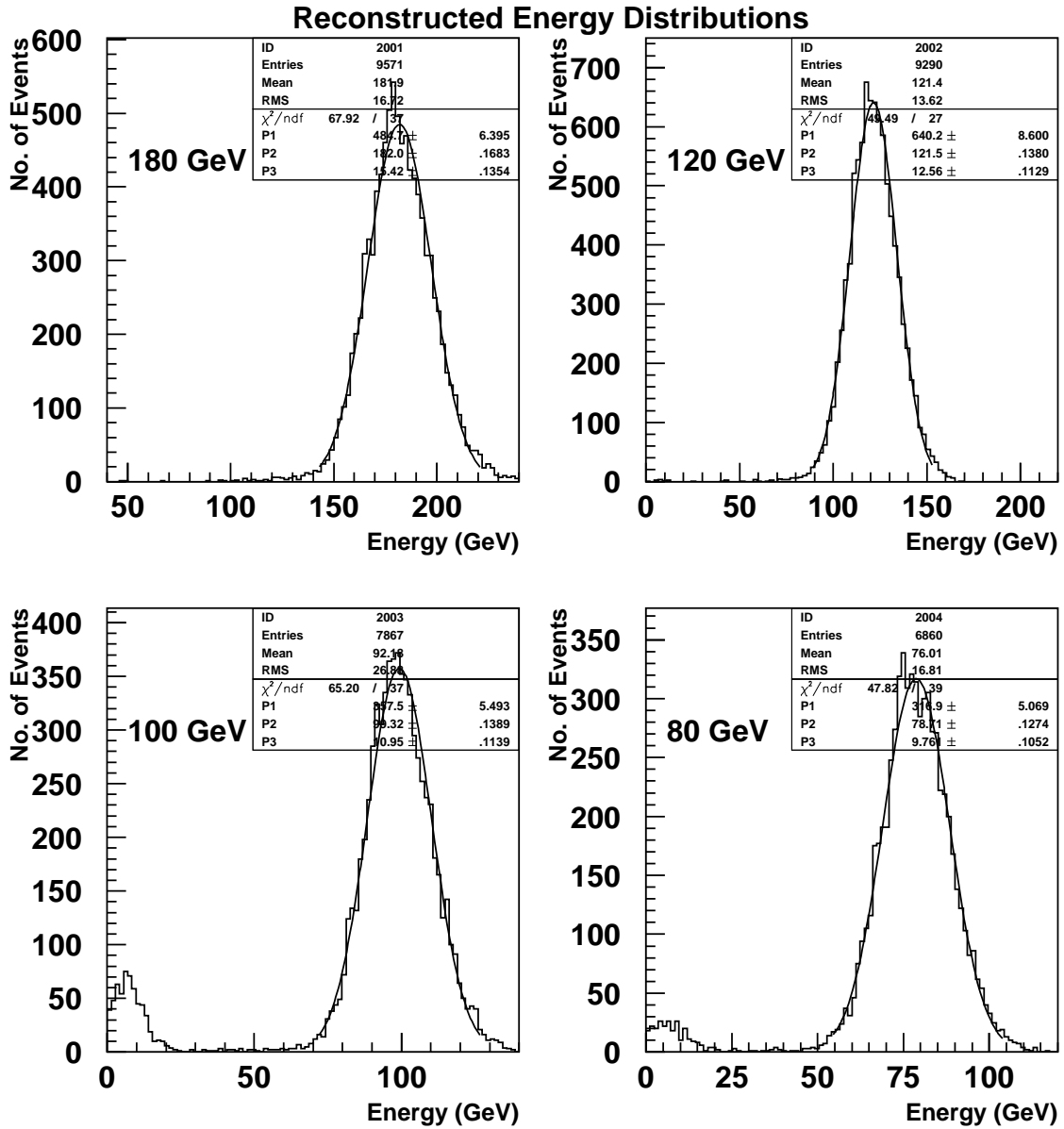


Figure 16: Pion cluster energy distributions for a typical impact point (H) after cuts and application of simple depth constants, beam energies 180 to 80 GeV. Muon contamination in the sample due to inefficiencies in the trigger and signal shape cuts can be observed at low energy, particularly for the 100 and 80 GeV beams.

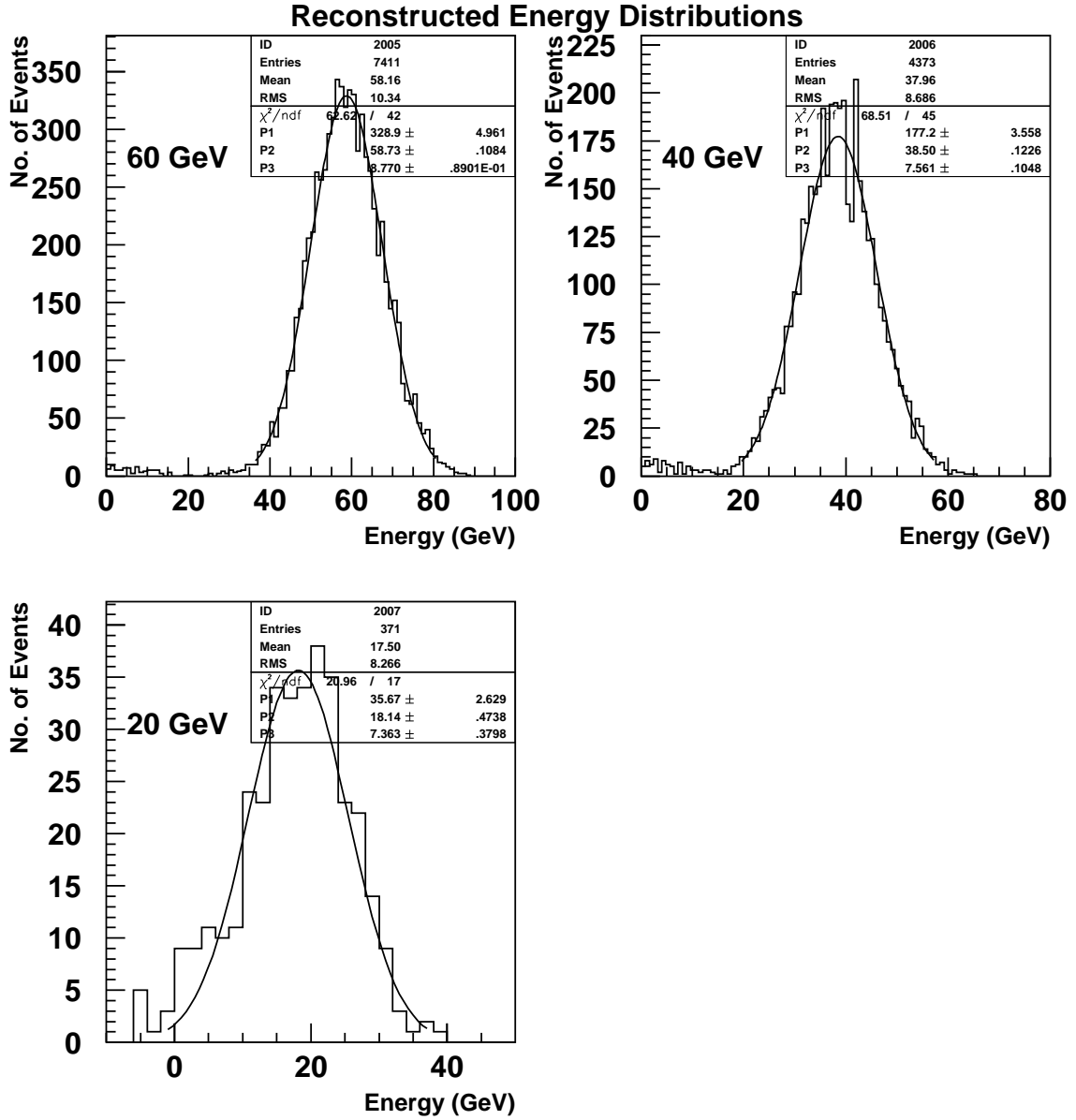


Figure 17: Pion cluster energy distributions for a typical impact point (H) after cuts and application of simple depth constants, beam energies 60 to 20 GeV.

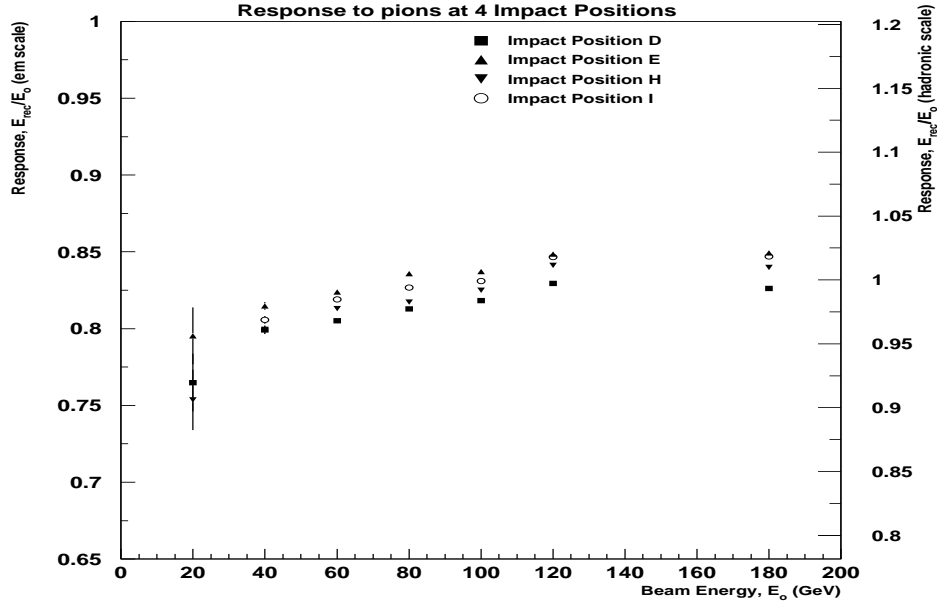


Figure 18: Pion response vs. energy is shown with two vertical scales. The scale on the left uses the electromagnetic scale constant (α_{em} as determined from electron data) while the scale on the right uses the hadronic scale constant (α_{had} as determined from pion data).

as a measurement of electronic noise. This measurement implicitly includes all correlations between individual cells. For 39 cell clusters at impact positions D, E, H and I the average noise is listed in the table below.

Impact Position	Average Electronic Noise (GeV)
D	6.38 ± 0.08
E	5.80 ± 0.06
H	5.69 ± 0.07
I	5.71 ± 0.07

10.4 Response to Pions

The response to pions over the energy range 20 to 180 GeV is shown in Figure 18. The left axis shows the response plotted on an electromagnetic scale (α_{em}) which contains information about the degree of non-compensation in the calorimeter (i.e. intrinsic e/h). The right axis shows the response using a global hadronic scale, α_{had} . The shape of the response curve is as expected for a non-compensating calorimeter with intrinsic e/h greater than one.

10.4.1 Electron to Hadron Response Ratio

A measurement of the intrinsic e/h can be extracted from Figure 18 by making use of the parameterizations for the electromagnetic fractional component F_{π^0} in a hadronic shower presented in Equations 2 & 3. The total visible energy for a hadron shower may be written in terms of the electromagnetic fraction F_{π^0} and the hadronic fraction $F_h = 1 - F_{\pi^0}$

$$E_{\text{vis}}^{\pi} = \langle E_{\text{vis}}^e \rangle + \langle E_{\text{vis}}^h \rangle = eF_{\pi^0}E + hF_hE \quad (15)$$

where E is the incident particle energy, e is the response to electrons, and h is the response to the purely hadronic component of a hadron shower.

Using this notation, the ratio of response to electrons and hadrons $\frac{e}{\pi}$ can be written

$$\frac{e}{\pi} = \frac{\frac{E_{\text{vis}}^e}{E_{\text{dep}}^e}}{\frac{E_{\text{vis}}^{\pi}}{E_{\text{dep}}^{\pi}}} = \frac{\frac{E_{\text{vis}}^e}{E_o^e}}{\frac{E_{\text{vis}}^{\pi}}{C_{\text{MC}}E_o^{\pi}}} \quad (16)$$

where C_{MC} is a correction factor which is applied to E_o^{π} to approximate E_{dep}^{π} accounting for leakage of the pion shower out of the calorimeter. It is calculated by Monte Carlo simulations [16]. Using $E_{\text{vis}}^e = eE$ and Equation 15, this can be rewritten

$$\frac{e}{\pi} = C_{\text{MC}} \times \frac{1}{F_{\pi^0} + \frac{h}{e}(1 - F_{\pi^0})} \quad (17)$$

where F_{π^0} is given in the parameterizations of Equations 2 & 3.

Figure 19 shows the fractional longitudinal, lateral, and total leakage out of the HEC for pion beams as obtained from the Monte Carlo simulation. Total leakage of 4.5% is typical, where the majority comes from lateral leakage. The Monte Carlo correction factors C_{MC} are calculated by subtracting the total leakage from unity. Figure 20 shows the Monte Carlo corrected e/π curve for impact position D. The curve is fit using the Wigmans and Groom¹⁷ parameterizations for F_{π^0} given in Equations 2 & 3 respectively. Monte Carlo simulations are only available for impact positions D & I. The results for these impact points are tabulated below.

Position	Wigmans Param. (Eqn.2)		Groom Param. (Eqn.3)	
	e/h	k	e/h	m
D	1.53 ± 0.06	0.10 ± 0.01	1.69 ± 0.07	0.83 ± 0.02
I	1.50 ± 0.09	0.10 ± 0.02	1.65 ± 0.09	0.83 ± 0.02
Average	1.52 ± 0.05		1.67 ± 0.06	

The results are in good agreement over the two impact positions, but the two parameterizations give slightly differing results¹⁸.

¹⁷The E_{scale} parameter in Equation 3 is fixed to 1 GeV, which is common in the literature. Varying E_{scale} produces effects in $\frac{e}{h}$ of the order of the statistical error.

¹⁸Differing results from the two parameterizations are common in the literature, and both results are usually quoted.

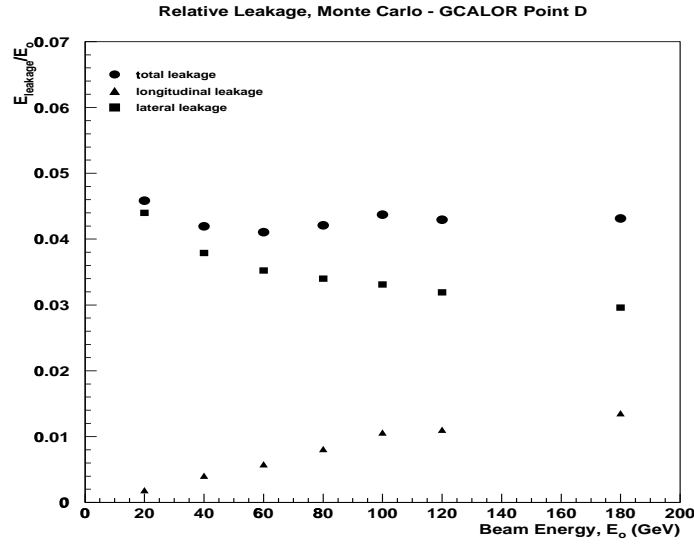


Figure 19: Fractional longitudinal, lateral, and total leakage out of the HEC for pion beams as obtained from the Monte Carlo hadronic shower simulation package GCALOR [16].

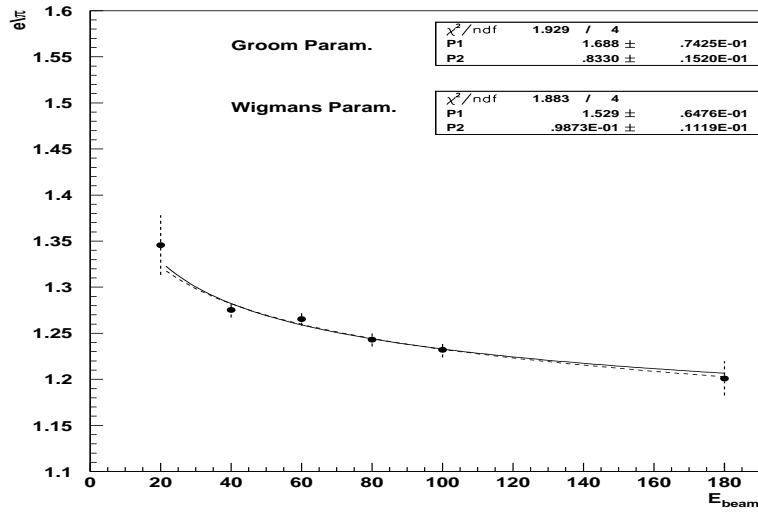


Figure 20: Monte Carlo corrected e/π curve for impact position D fit using the Wigmans and Groom parameterizations for F_{π^0} .

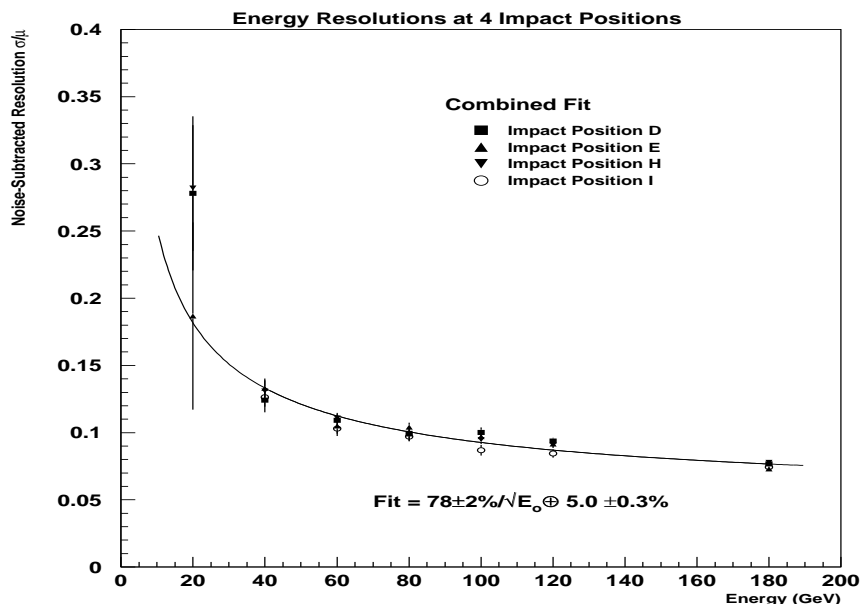


Figure 21: Energy resolution fit over four impact positions for a 39 cell cluster and simple depth constants.

10.5 Pion Energy Resolution

As discussed previously (Section 10.3), the electronic noise in a cluster of cells can be independently measured using random trigger events. Once this has been measured for a given cluster its influence can be removed and the parameterization of Equation 7 can be re-written:

$$\frac{\sigma}{E} = \frac{A}{\sqrt{E_0}} \oplus B \quad (18)$$

where A and B are the sampling and constant terms respectively.

Figure 21 shows the noise-subtracted resolution as a function of energy for 4 different impact positions for a 39 cell cluster and simple depth constants. Consistency between impact points is evident despite the high voltage problems in one of the modules. The adjustment of the simple depth constants effectively compensates for the loss of signal.

The results of fits to data for each of the four impact positions is tabulated below.

Position	A(% $\text{GeV}^{\frac{1}{2}}$)	B(%)	χ^2/ndf
Module 1			
D	77 ± 4	5.5 ± 0.5	2.5
H	84 ± 4	5.4 ± 0.4	1.3
Module 2			
E	77 ± 4	4.2 ± 0.6	2.0
I	73 ± 4	5.0 ± 0.4	1.3

A combined fit of equation 18 to the data for 4 impact positions yields the result

$$\frac{\sigma}{E} = \frac{78 \pm 2\%}{\sqrt{E_o}} \oplus 5.0 \pm 0.3\%, \quad \frac{\chi^2}{\text{ndf}} = 1.9 \quad (19)$$

using a 2.5σ Gaussian fit on the reconstructed energy distributions. Results for 2σ and 3σ fits have also been obtained and lead to very similar resolutions at all beam energies with sampling and constant terms consistent within error.

11 Considerations for the Reconstruction of Hadronic Showers with the HEC in ATLAS

In the ATLAS environment, the HEC will sit directly behind the Electromagnetic Endcap Calorimeter (EMEC). As such, individual particles will begin showering before reaching the HEC. Energy measurements will be made with clusters including cells from both the EMEC and the HEC. Since the EMEC has significantly finer segmentation and achieves better energy resolution, the combined energy resolution of the two calorimeters is expected to improve significantly over that of the HEC alone. Though the size of a cluster necessary to contain jets will be larger than that for single pions, HEC's pointing geometry will reduce that size as compared to the situation at the beam tests where the pointing geometry was not exploited.

The uncertainty to which a pion's energy can be reconstructed from a measurement using the calorimeter is different than the energy resolution. Given a measurement of the incident particle energy, there is a non-Gaussian curve which describes the probability the measurement originated from a particle of a given incident energy. This curve (derived from the pion energy resolution parameterization of Equation 19) is shown in Figure 22 for a reconstructed energy measurement of 100 GeV. The root mean square of this curve is about 12 GeV, which gives an indication of the accuracy to which the energy of an individual pion can be reconstructed. If measurements of incident particle energy are made by more than one subdetector (i.e. the inner detector and the EMEC/HEC combination) curves such as this need be considered from all measurements to determine the most probable reconstructed energy.

12 Conclusions

The first Hadronic Endcap modules built to the final ATLAS specifications were successfully tested in April 1998.

Using a 3 cell cluster, the response to electrons is found to be constant to within 1%. A combined fit over all impact positions produces the following parameterization for the energy resolution (E_o in GeV):

$$\frac{\sigma}{E} = \frac{22.0 \pm 0.1\%}{\sqrt{E_o}} \oplus 0.0 \pm 0.2\% \oplus \frac{0.54 \pm 0.02}{E} .$$

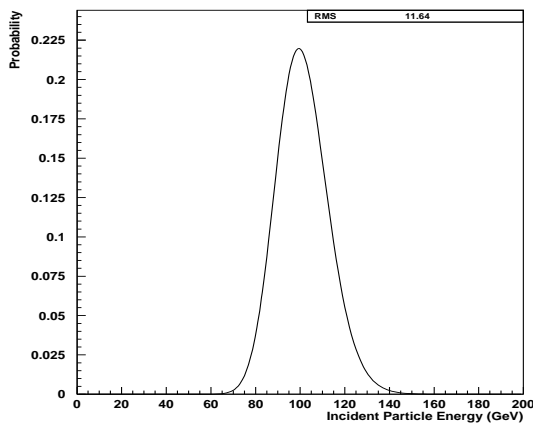


Figure 22: Probability a reconstructed incident particle energy of 100 GeV originated from a particle of a given incident energy.

The electron to muon response ratio is evaluated as

$$\frac{e}{\mu_{120\text{GeV}}} = 0.96 \pm 0.03 \quad (20)$$

and is evolved down to mip energies to give an estimate of the electron to mip response, $\frac{e}{\text{mip}} \simeq 0.83$. Both of these ratios involve Monte Carlo predictions.

Large clusters and simple depth constants are used to extract calorimeter parameters from pion data. The response to pions follows the expected behaviour for a non-compensating calorimeter with electron to hadron response ratio greater than one.

The $\frac{e}{h}$ ratio, after correcting for leakage with Monte Carlo simulations, is

$$\frac{e}{h}|_{\text{Wigmans}} = 1.52 \pm 0.05 \quad (21)$$

$$\frac{e}{h}|_{\text{Groom}} = 1.65 \pm 0.09 \quad (22)$$

using the Wigmans (Equation 2) and Groom (Equation 3) parameterizations for F_{π^0} respectively.

The energy resolution can be parameterized as

$$\frac{\sigma}{E} = \frac{78 \pm 2\%}{\sqrt{E_o}} \oplus 5.0 \pm 0.3\%$$

from a combined fit over data from four impact positions. The performance at all four impact positions studied are comparable after the application of simple depth constants to compensate for high voltage problems in module 2.

References

- [1] Dobbs, Matt, Lefebvre, Michel, & O'Neil, Dugan, *Hadronic Endcap Modules Zero Pion and Electron Energy Scan Analysis from April 1998 Testbeam Data*, ATLAS Internal Note ATL-LARG-99-001, ATL-COM-LARG-98-009, HEC-Note-59, November 23, 1998.
- [2] Griffiths, D., **Introduction to Elementary Particles**, Wiley, 1987.
Godfrey, S., *The Standard Model and Beyond*, Physics in Canada, Vol. 50, No. 2, p. 108 (1994).
- [3] The ATLAS Collaboration, Technical Proposal, CERN/LHCC/94-43, 15 December 1994.
- [4] The ATLAS Collaboration, Liquid Argon Technical Design Report CERN/LHCC 96-41.
- [5] The ATLAS Collaboration, **Technical Design Reports**,
Calorimeter Performance Technical Design Report CERN/LHCC 96-40
Computing Technical Proposal CERN/LHCC 96-43
DAQ, EF, LVLE2 and DCS Technical Progress Report CERN/LHCC 98-16
Inner Detector Technical Design Report CERN/LHCC 97-16 & CERN/LHCC 97-17
Level 1 Trigger Technical Design Report CERN/LHCC 98-14
Muon Spectrometer CERN/LHCC 97-22
Tile Calorimeter Technical Design Report CERN/LHCC 96-42
Trigger Performance Status Report CERN/LHCC 98-15
- [6] Particle Data Group, *Review of Particle Physics*, European Physical Journal C, Vol. 3, No. 1-4, 1998.
- [7] EGS4 has emerged as the standard Monte Carlo.
Nelson *et al.*, *The EGS4 Code System*, SLAC-265 (1985).
- [8] Wigmans, Richard, *On the Energy Resolution of Uranium and Other Hadron Calorimeters*, CERN/EP 86-18 (1986), Nucl. Instr. Meth. A259 (1987) 389.
- [9] Gabriel, T.A., Groom, D.E., Job, P.K., Mokhov, N.V., and Stevenson G.R., *Energy dependence of hadronic activity*, Nucl. Instr. Meth. A338 (1994) 336.
- [10] Amaldi, Ugo, *Physica Scripta*, Vol. 23 (1981) 409-424.
- [11] Groom, D.E. *Four-Component Approximation to Calorimeter Resolution*, Proceedings of the 2nd International Conference on Calorimetry in High Energy Physics, Capri, Italy, October 14-18, 1991.
- [12] ATLAS - HEC Collaboration, *Electron and Pion Test Beam Data Analysis of the Hadronic Endcap Prototype Calorimeter*, ATLAS Liquid Argon Note No. 95, April 16, 1998.
- [13] De La Taille, D., and Serin, L., LARG-NO-29, November 1995.

- [14] Cleland, W.E. and Stern, E.G., *Signal processing considerations for liquid ionization calorimeters in a high rate environment*, Nuclear Instruments and Methods in Physics Research, A338 (1994) 467-497.
- [15] The Tile Calorimeter Collaboration, *Response of the ATLAS Tile Calorimeter Prototype to Muons*, CERN-PPE/96-173.
- [16] Monte Carlo simulations of the HEC calorimeter are performed by the HEC Simulation Group using the GEANT3 software package.
Kiryunin, A.E., and Salihagić, *Monte Carlo for the HEC Prototype: Software and Examples of Analysis*, HEC Note-063 (1998).
R. Brun et al., *GEANT3*, CERN/DD/EE/84-1 (1986).